

Near-surface Clay Sediments: Self-assembly and Response to Ionic Concentration Gradients

Mengwei Liu* and J. Carlos Santamarina*

Affiliations: *School of Civil and Environmental Engineering, Georgia Institute of Technology, Atlanta, GA 30332, United States (Formerly at KAUST).

Corresponding author: Mengwei Liu (liumw.zr@gmail.com)

Abstract: Clay self-assembly, fabric formation and fabric changes are governed by mineral composition, pore fluid pH and ionic strength. This study combines theoretical analyses, extensive data compilation and targeted experiments to investigate underlying processes. Experiments include sedimentation-diffusion tests combined with multi-physics monitoring, including micro-CT, optical and acoustic imaging, grazing-incidence X-ray diffraction and nuclear magnetic resonance NMR spectroscopy. Updated fabric maps for 1:1 kaolinite and 2:1 montmorillonite reveal distinct particle associations within the pH–ionic concentration space delineated by well-defined thresholds. The initial void ratio e_0 at the onset of sediment formation is primarily controlled by specific surface area, and is higher than the void ratio at the liquid limit; hence, soft sediments may swell towards e_0 when flooded - even with brine. Unconstrained fine particles can migrate against ionic concentration gradients (diffusiophoresis), while dense packings hinder ionic diffusion by excluding transport through narrow pore-throats. Salt diffusion causes volumetric strain but with minimal fabric changes, underscoring the stability of self-assembled networks. Vertical and horizontal discontinuities may form during ionic diffusion, often nucleating at grain-displacive bubbles formed from excluded gas. These processes help explain phenomena such as soil dispersion, quick clay formation, surface erosion, clogging, and clay liner degradation under leachate exposure.

Keywords: Clays; Fabric/structure of soils; Particle-scale behaviour.

List of Notations

A [J]	Hamaker constant
c [mol/L]	Pore fluid ionic concentration
d [m]	Interparticle distance (Accent: \bar{d} = mean value)
d_{ion} [m]	Diameter of diffusing ion
D [m ² /s]	Diffusion coefficient (Subscripts: a = apparent diffusion, 0= self-diffusion)
e	Void ratio (Subscripts: ∞ = asymptote at high effective stress, 0= asymptote at low effective stress, i= initial, LL= at the liquid limit, max= maximum, 1kPa = at an effective stress of 1kPa)
F [C/mol]	Faraday constant
G_s	Specific gravity
h [m]	Particle thickness
R [J/(K · mol)]	Gas constant
S_s [m ² /g]	Specific surface area
t [sec]	Time
T [K]	Temperature
U [J/m ²]	Interaction energy per unit area (Superscripts: vdw= van deer Waals, ddl= diffusive double layer)
z	Valence
α	Exponent used in diffusion model
ε_{vol}	Volumetric strain
ε_o [F/m]	Permittivity of free space
ε	Relative permittivity of the pore fluid
λ_D [m]	Debye length
η	Exponent used in consolidation model
ρ [kg/m ³]	Density (Subscript: w= water)
θ	Angle between the incident rays and the diffracting planes
σ' [kPa]	Effective stress (Subscripts: c= characteristic value in consolidation model)
Θ	Path tortuosity
Ψ [V]	Surface potential (Subscript: 1= 1 st interacting face, 2= 2 nd interacting face; Stern= Stern potential)

INTRODUCTION

Clays are phyllosilicate minerals characterized by particles in the micron to submicron size range. Their self-assembly and fabric formation are governed by factors such as particle thickness, mineral composition, pore fluid pH, and the type and concentration of dissolved ions((van Olphen 1964, O'Brien 1971, Rand and Melton 1977, Santamarina et al. 2001, Gupta et al. 2011, Chang et al. 2021) – Note: Throughout this manuscript, the term “clay” refers specifically to mineralogy and implies particles of micron and submicron size).

Young, soft clay sediments exposed to concentration gradients and changes in pore fluid chemistry undergo coupled chemo-hydro-mechanical processes (Collins and McGown 1974, Barbour 1987, Santamarina and Fam 1995, Di Maio 1996, Musso et al. 2022). Field examples include freshwater clay slurries resting on top of saltwater (Schroeder et al. 2015), Norwegian illitic clay instability after ion leaching (Rosenqvist 1953), saltwater intrusion along coastlines (Randolph and Gourvenec 2017), salt flats atop sediments (Goodall et al. 2000), desalination plant discharge onto clay sediments (Roberts et al. 2010), and “freshening” during gas hydrate disassociation (Riboulot et al. 2018).

The complex chemo-hydro-mechanical interactions between clay sediments and pore fluids become most pronounced as skeletal forces diminish as the effective stress approaches zero $\sigma' \rightarrow 0$. In this context, the present study revisits the self-assembly of clay particles and examines the response of near-surface clay sediments to concentration gradients. The manuscript begins with a description of the methodology, followed by an investigation of clay particle self-assembly and their response to ionic concentration gradients.

METHODOLOGY

This research integrates physical analysis, particle-to-macro scale experimental techniques, and extensive data compilation to investigate the underlying processes. The following sections provide detailed descriptions of the multi-physics characterization methods employed in the study.

Asymptotic void ratio

The void ratio near the sediment-water interface reflects particle self-assembly during the initial formation of the granular skeleton. In this study, we measured the asymptotic void ratio of a Na-bentonite, included previously gathered data on kaolinite and illite from our group, and compiled complementary data from the literature including sands and silts. The tested Na-bentonite (sourced from Euclid's Pottery Store, USA; liquid limit $LL=360$, specific surface area $S_s=550\text{ m}^2/\text{g}$; main clay mineral: montmorillonite) was mixed with NaCl solutions at nine different ionic concentrations (0.05 to 4 mol/L, with 50 g bentonite per litre of solution). The suspensions were allowed to settle in flat bottom flasks until they reached a stable height which was then used to calculate e_0 . The use of high specific surface area bentonite in this and other experiments in this study is intended to emphasize the physicochemical effects under investigation, as discussed in the following section.

Particle migration in an ionic concentration gradient

Diffusiophoresis refers to the migration of molecules and colloidal particles in response to a concentration gradient (Prieve et al. 1984, Ebel et al. 1988, Anderson 1989). To investigate the potential for this phenomenon in clay systems, we introduced a salt crystal into a 3 mm-thick layer of a stable bentonite-water mix, contained in a sealed petri dish (50 g/L in deionized water; initial void ratio $e_i = 53$). The dish sat on a light table beneath a 24-megapixel camera (Figure 1a). Although individual particles were not optically resolvable, fines migration was inferred from changes in opacity over time, captured through time-lapse photography.

Changes in interplatelet separation caused by a concentration front

Grazing Incidence X-Ray Diffraction GI-XRD was used to obtain platelet-scale structural information during diffusion. GI-XRD is a surface-sensitive X-ray diffraction technique in which the incident beam strikes the sample at a shallow angle, minimizing penetration depth and enhancing sensitivity to near-surface features. It is commonly applied for structural characterization and the assessment of strains in thin films. In this study, a deaired bentonite slurry (50 g of clay per liter of deionized water) was prepared and then flooded with a 0.25 M NaCl solution. The specimen was analyzed using small-angle GI-XRD at a grazing angle of 0.5° , with a radiation wavelength of 1.54 \AA and an angular resolution of $2\Delta\theta = 0.01^\circ$ (Figure 1b - Bruker D8 Discover system with Cu $K\alpha$ radiation, equipped with a multimode Eiger2R 500K 2D detector). The 2D detector enabled the capture of diffraction patterns over the full azimuthal range ($0-180^\circ$), allowing interparticle spacing to be inferred in all directions. The spacing values were then obtained by radially integrating the signals across the entire angular span.

Internal processes during brine flooding

Time-lapsed X-ray microtomography was employed to investigate subsurface processes following the flooding of a soft sediment with a 0.25 M NaCl solution (Figure 1c. Bentonite specimen with initial void ratio of $e_i=53$ contained within a 25 mm diameter glass tube. MicroCT: TESCAN CoreTOM). Due to the voxel size of $42 \text{ }\mu\text{m}$, microCT imaging could not resolve individual clay particles. However, the natural bentonite contained high-density impurities that appear as bright spots in the 3D tomograms. These impurities served as tracers enabling digital image correlation analysis between successive tomograms (software: particle image velocimetry PIV plugin in ImageJ). Identical tests were performed using both a standard bentonite mixture and an extensively deaired mixture to assess the role of gas bubbles in nucleating internal discontinuities.

Changes in pore size distribution due to an increase in salt concentration

Nuclear magnetic resonance NMR spectra for water-soil mixtures primarily reflect surface relaxation as diffusing water molecules interact with mineral surfaces; the characteristic relaxation times are indicative

of the diffusion length and are directly related to pore size. In this study, a deaired bentonite slurry was prepared using deionized water to investigate changes in pore size distribution following surface flooding with a 0.25 M NaCl solution gently added to the top of the specimen (Figure 1d. Specimen: initial void ratio of $e_i=53$, placed in a glass tube of 25 mm diameter); successive T_2 relaxation spectra were acquired over time to monitor changes induced by salt diffusion (12 MHz Oxford Instruments). For reference, two additional bentonite specimens were prepared by thoroughly mixing equal volumes of bentonite slurry with either deionized water or a 1 M NaCl brine. In both cases, NMR spectra were recorded after the sediments had stabilized (Figure 1e).

Large-scale effects caused by ionic diffusion

Finally, the macroscale response of a soft bentonite sediment was investigated using a large cylindrical Plexiglas tank designed to minimize boundary effects (diameter: 500 mm; Figure 1f). The sediment was prepared by mixing bentonite with deionized water at a concentration of 50 g/L, resulting in an initial void ratio of $e_i=53$. The experiment was instrumented with piezocrystals for acoustic reflection monitoring (Crystals: high-damping water-coupled 400 kHz P-wave crystals, immersed 5 mm into the overlying brine layer. Input signal: square wave with a 50 ms period for effective signal stacking. Details in (Lee and Santamarina 2005, Liu et al. 2024)). High-resolution cameras were positioned to capture time-lapse images of both the sediment surface and the sediment-brine interface (Figure 1f). The bentonite slurry was placed into the tank and allowed to rest for 24 hours before a 0.25 M NaCl brine solution was carefully added on top (the entire flooding process took 60 minutes). P-wave signals and photographic data were collected at regular intervals throughout the 24-day experiment.

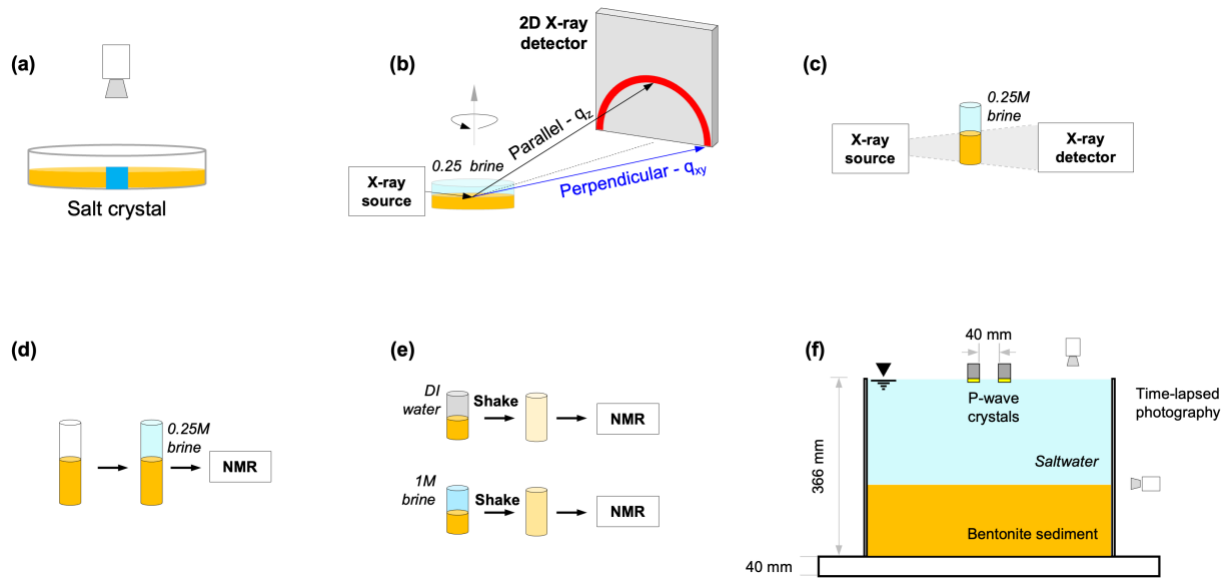


Figure 1. Multiphysics experimental setups used to investigate clay behavior under ionic concentration gradients. (a) Time-lapse photography: clay particle migration in an ionic concentration gradient - diffusiophoresis. (b) Grazing incidence X-ray diffraction GI-XRD: platelet-scale structural changes at the brine-sediment interface. (c) Time-lapsed X-ray microtomography: subsurface processes following the flooding of a soft sediment with brine. (d, e) Nuclear magnetic resonance NMR: <d> changes in pore size distribution under diffusion and <e> after mixing. (f) Large-size sediment tank instrumented with high resolution acoustic monitoring system and time lapse photography. All tests started with a bentonite slurry prepared at a void ratio $e=53$.

SELF-ASSEMBLY

Clay particles tend to aggregate as they settle through the water column or within soil pore spaces during diagenetic dissolution-precipitation processes. Their self-assembly is governed by mineral characteristics and pore fluid chemistry, and it defines the *ab initio* void ratio at virtually zero effective stress.

Self-assembly: Mineral characteristics and pore fluid chemistry

This section analyses particle self-assembly by combining Derjaguin–Landau–Verwey–Overbeek DLVO theory with published nanometre-scale experimental data gathered using atomic force microscopy AFM (by Chang et al. 2021) and platelet-scale numerical simulation results (Bourg et al. 2007). The new results provide particle-scale insight to the fabric map defined in the pH-concentration space generated from macroscale experimental studies reported earlier (Santamarina et al. 2001).

DLVO analysis. The interaction energy per unit area U [J/m^2] = $U^{vdw} + U^{ddl}$ considers van der Waals attraction U^{vdw} and double layer repulsion U^{ddl} . The van der Waals attraction per unit area as a function of the interparticle distance d is (Israelachvili 2011),

$$U^{vdw} = -\frac{A}{12\pi d^2} \quad (1)$$

where the Hamaker constant A [J] depends on the properties of the mineral surfaces and the polarizability of the intervening fluid (permittivity), but it is quite insensitive to the fluid's electrical conductivity (ionic strength - See Lifshitz theory and experimental evidence in van Olphen 1964, Israelachvili 1978, Elzbieciak-Wodka et al. 2014, Valmacco et al. 2016). The Hamaker constant for common clay minerals in water - including kaolinite, illite, and montmorillonite - ranges from 5×10^{-21} to 10×10^{-21} J, and it increases by an order of magnitude in dry clays (Santamarina and Fam 1995, Bergström 1997, Weber and Kaufhold 2021).

The double layer repulsion between clay surfaces depends on the surface potentials Ψ_1 and Ψ_2 [V] of the two interacting faces (Kar et al. 1973, Masliyeh and Bhattacharjee 2006),

$$U^{ddl} = \frac{\varepsilon\varepsilon_0}{2\lambda_D} \left\{ (\Psi_1^2 + \Psi_2^2) \left[1 - \coth\left(\frac{d}{\lambda_D}\right) \right] + 2\Psi_1\Psi_2 \operatorname{cosech}\left(\frac{d}{\lambda_D}\right) \right\} \quad (2)$$

where material parameters include the permittivity of free space ε_0 [F/m], the relative permittivity of the pore fluid ε , and the Debye length or “double layer thickness” λ_D [m] that is a function of the pore fluid ionic concentration c [mol/L] and valence z (Mitchell and Soga 2005, Israelachvili 2011):

$$\lambda_D = \sqrt{\frac{\varepsilon_0\varepsilon RT}{2F^2 c z^2}} \quad (3)$$

The remaining parameters are the Faraday constant $F = 96500$ C/mol, the gas constant $R = 8.314$ J/(K · mol), and temperature T [K].

The Stern potential Ψ_{Stern} [V] is adopted to compute the interaction between clay platelets in Equation 2. Measured Stern potentials using atomic force microscopy AFM at various pH levels and low ionic concentration show small changes in the Si-layer, but pH-dependent charges for the Al-layer and edges (See Figure S1 in the Supplementary Information). These experimental observations confirm that the charge of the Si-layer is primarily determined by isomorphic substitution, whereas the charge of the Al-layer is controlled by pH-dependent protonation-deprotonation surface reactions.

Kaolinite. Kaolinite is a 1:1 platy clay mineral with two distinct surfaces; the gibbsite layer is an alumina octahedral sheet with exposed hydroxides OH, and the silica layer is a tetrahedral sheet with exposed oxygen O atoms. Consequently, both faces exhibit distinct interactions with the surrounding pore fluid. Then, six possible self-assembly configurations can take place among kaolinite particles: edge-to-edge, edge-to-face (either Al-face or Si-face), and face-to-face (Al-Al, Si-Si, and Si-Al).

Then, the interaction energies for the six potential fabrics are computed to anticipate the potential self-assemblies as a function of pH and ionic concentration. The analysis of edge-to-face interaction assumes “thick particles” where the particle thickness is greater than the Debye length, $h > \lambda_D$ (Note: for kaolinite, $h=100$ -to- 500 nm). We identify possible particle associations by computing the interaction energy at a distance $d \approx 2\lambda_D$. Assuming the surface and edge charges are concentration independent (Gupta and Miller

2010, Liu et al. 2014, Mohammed et al. 2021), van der Waals attraction prevails when the ionic concentration exceeds ~ 0.1 mol/L. On the other hand, the pH-dependent fabric transitions are selected at the points of zero charge: pH = 6.5 for the Al-face, pH = 5 for edges and pH < 2 for the Si-face (see Figure S1).

Finally, the fabric map in Figure 2a identifies the most likely associations for kaolinite particles in the pH-concentration space. At **low ionic concentration** $c \leq \sim 0.1$ mol/L and **acidic conditions** (e.g. young landfills, acid rain, forest soils and podzols): the Al-face to Si-face association is most common for a wide range of acidic conditions pH < 6.5, edge-to-Al face prevails at $5 < \text{pH} < 6.5$, and edge-to-Si layer takes place at lower pH < 5; expect extensive mineral dissolution and buffering in very acidic conditions (e.g. acid mine drainage, pyrite exposure to water and oxygen forming sulfuric acid, volcanic and hydrothermal systems). At **low ionic concentration** $c \leq \sim 0.1$ mol/L and **alkaline conditions** (pH > 6.5; e.g. mature and old landfills, carbonate buffering in arid and semi-arid soils, agricultural fields treated with lime, saline-alkali water): particles remain dispersed, and even Al-Si face-to-face association is unlikely. At **high ionic concentration** $c \geq \sim 0.1$ mol/L: surface charges are shielded, van der Waals attraction prevails and most particle associations can form; while a repulsion barrier remains between Si-face-to-Si-face associations, elevated ionic concentrations can sufficiently screen this repulsion to allow particles to approach closely enough for tactoid formation. The resulting fabric map in Figure 2a resembles the map inferred from macro-scale experiments (Palomino and Santamarina 2005), but it identifies distinct face-specific associations for 1:1 kaolinite, and adopts well-defined pH and ionic concentration thresholds.

Montmorillonite (Note: Although tests are conducted using natural bentonite, this analysis focuses on the pure clay mineral montmorillonite). In contrast to kaolinite, montmorillonite is a 2:1 clay with two silicate surfaces; therefore it can self-assemble in only three configurations: edge-to-edge, edge-to-face and face-to-face. At **low ionic concentration** $c < \sim 0.25$ mol/L: faces are equally charged and double layer repulsion hinders face-to-face aggregation (regardless of pH); the edge charge transitions from negative to positive at pH ≈ 5 -to-5.5 (Bourg et al. 2007 – See Figure S1 in Supplementary Information), however, the face double

layer thickness exceeds the thin montmorillonite plate thickness $\lambda_D > h \approx 1 \text{ nm}$ when $c < 0.1 \text{ mol/L}$ (Bourg et al. 2007), and the electrostatic potential spillover effectively hides the edge charge, limiting edge-to-face interactions. At **high ionic concentration** $c > \sim 0.25 \text{ mol/L}$: surface and edge charges are screened, double-layer repulsion fades, and edge-to-edge and edge-to-face interactions become possible. While face-to-face aggregation is hindered by like charges, the high ionic concentration in the pore fluid allows for parallel particle arrangements in close proximity. The resulting fabric map is summarized in Figure 2b.

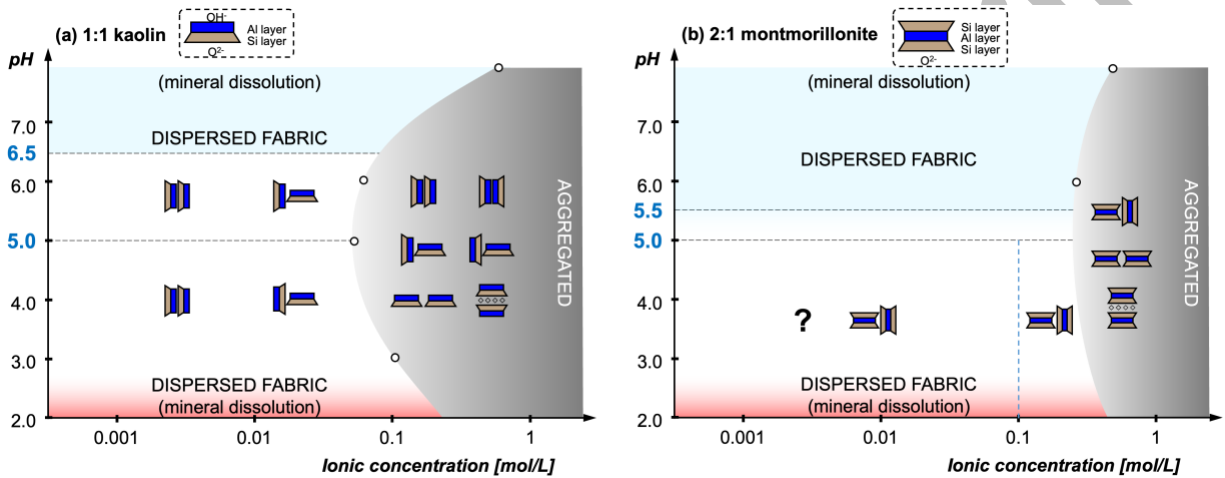


Figure 2. Fabric maps for kaolinite and montmorillonite computed from published AFM data and platelet-scale numerical simulation results. (a) 1:1 Kaolinite. (b) 2:1 Na-montmorillonite. Open circles: predicted concentration thresholds using DLVO analysis. Horizontal dashed lines at low concentration: pH thresholds from AFM measurements (Chang et al. 2021) and simulation results (Bourg et al. 2007), summarized in the Supplementary Figure S1. For comparison, see original fabric maps inferred from macroscale observations in (Santamarina et al. 2001, 2002).

Suspension-to-sediment transition: Asymptotic void ratio

When does a suspension become a sediment? What is the *ab initio* void ratio at the onset of sediment formation? Suggested mechanistic criteria are based on large-strain viscosity behaviour (Rand and Melton 1977) or small-strain shear wave measurements (Klein and Santamarina 2005, Salva et al. 2023). An alternative approach is to identify the asymptotic void ratio during sedimentation, when effective stress emerges and begins to govern self-weight consolidation; this approach requires an asymptotically correct function to capture the evolution of void ratio e as a function of effective stress σ' [kPa]. The void ratio decreases with increasing effective stress, typically following exponential or power-law relationships (Hansen 1969, Bauer 1996). Consider the following exponential function (reformulated in (Chong and Santamarina 2016); application example in (Lyu et al. 2021)):

$$e = e_0 - (e_0 - e_\infty) \left\{ 1 - \exp \left[- \left(\frac{\sigma'}{\sigma_c'} \right)^\eta \right] \right\} \quad (4)$$

where e_0 is the asymptotic void ratio at the suspension-to-sediment transition $\sigma' \rightarrow 0$, and e_∞ is the asymptotic void ratio at very high effective stress in deep sedimentary basins; the two other fitting parameters are the characteristic effective stress σ_c' and the exponent η (often $\approx 1/3$).

Published sedimentation and consolidation data, along with newly obtained experimental results (as described above), were analysed to determine the asymptotic void ratio e_0 across a wide range of soils. Figure 3 plots the asymptotic void ratio e_0 versus the sediment specific surface area S_s [m^2/g]. The self-assembly of clayey soils is driven by electrical interactions and affected by pore fluid chemistry, as discussed above (Figure 2). Estimated void ratios for edge-to-face and face-to-face arrangements depend on specific surface area and slenderness; slenderness is positively correlated with specific surface area (Figure 3).

The void ratio e_{LL} at the liquid limit LL can be estimated using empirical equations that relate the liquid limit LL to the specific surface area S_s , assuming the soil is saturated at the liquid limit (Farrar and Coleman 1967). The estimated e_{LL} -vs- S_s trend superimposed on Figure 3 indicates that the asymptotic void ratio is higher than the void ratio at the liquid limit $e_0 > e_{LL}$ when sedimentation occurs in low ionic strength fluids;

conversely, data points below the e_{LL} line in Figure 3 represent clay sediments formed in high ionic concentration fluids, particularly in high specific surface area clays (details in (Salva et al. 2023)). Soil-water mixtures prepared below the asymptotic void ratio should swell when submerged in water; this implies that these mixtures should experience suction before flooding. Indeed, pastes prepared at the liquid limit typically exhibit a suction of approximately 6 kPa (Russell and Mickle 1970, Hong et al. 2010). Further supporting evidence comes from a data compilation showing that the void ratio e_{1kPa} at an effective stress of $\sigma' = 1 \text{ kPa}$ is approximately $e_{1kPa} \approx 1.25 \cdot e_{LL}$ (Chong and Santamarina 2016 – Note: the concept of “capillary confinement” is discussed later in the text).

For completeness, data for coarse-grained soils are included in Figure 3. The loose packing of mono-sized spheres $e = 0.91$ is shown for reference. Careful inspection of this dataset readily confirms the prevalent effects of particle shape and grain size distribution on packing density (Youd 1973, Cubrinovski and Ishihara 2002, Cho et al. 2006, Fuggle et al. 2014). Overall, the asymptotic void ratio increases with specific surface area even in silts; evidently, electrical interactions influence fabric formation in soils with specific surface areas as low as $S_s \approx 0.1 \text{ m}^2/\text{g}$ and above.

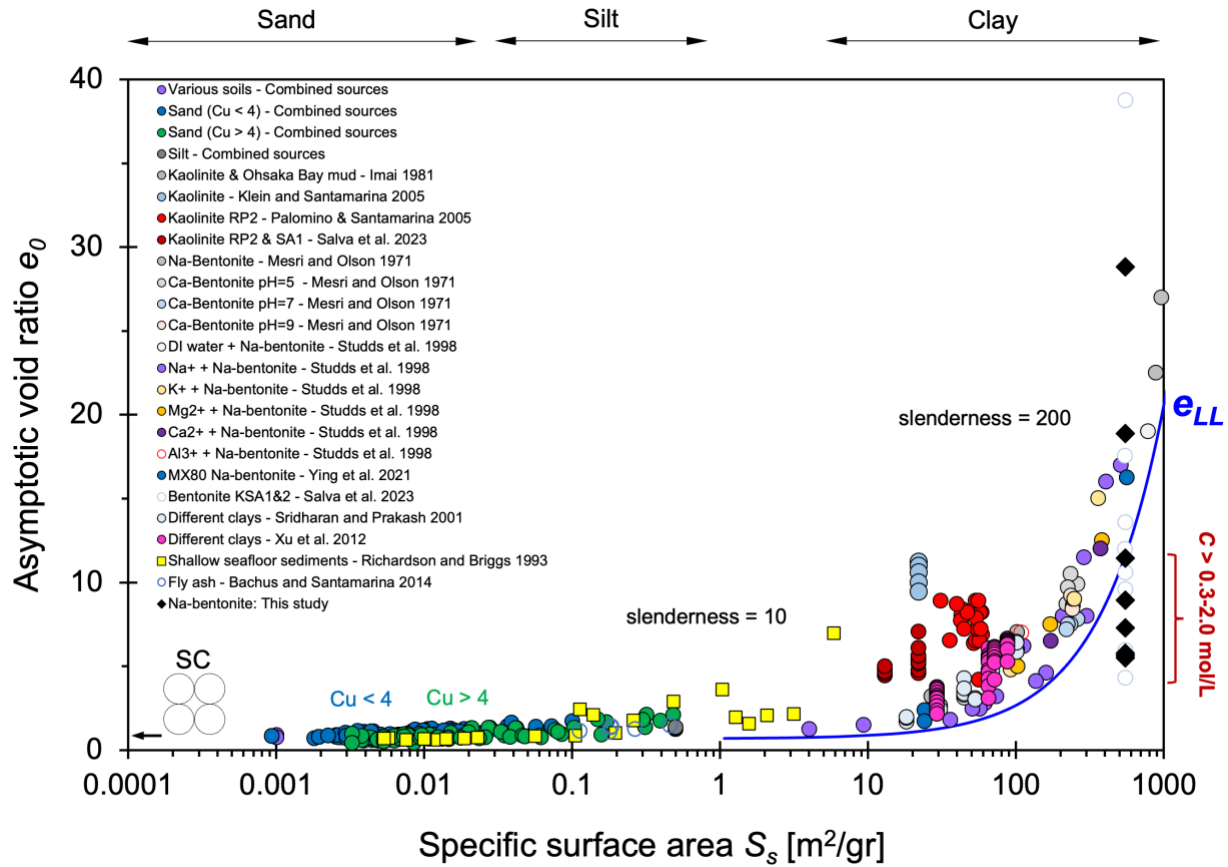


Figure 3. Asymptotic void ratio e_0 as a function of specific surface area S_s . Electrical interactions influence fabric formation in soils with specific surface areas as low as $S_s \approx 0.1 \text{ m}^2/\text{g}$ and above. Blue trend: void ratio at liquid limit e_{LL} estimated from LL -vs- S_s data in Farrar and Coleman (1967). Data sources: this study, (Mesri and Olson 1971, Imai 1981, Richardson and Briggs 1993, Studds et al. 1998, Sridharan and Prakash 2001, Klein and Santamarina 2005, Palomino and Santamarina 2005, Cho et al. 2006, Xu et al. 2012, Bachus and Santamarina 2014, Ying et al. 2021, Salva et al. 2023).

RESPONSE TO IONIC CONCENTRATION GRADIENT

The previous section examined the clay self-assembly process and quantified the resulting asymptotic void ratio across a broad range of soils, highlighting the critical role of specific surface area. Now, consider a clay fabric controlled by electrical interparticle interactions. Strains induced by changes in ionic strength are more pronounced when the diffuse double layer thickness λ_D (Equation 3) is significant relative to the platelet thickness h . Since specific surface area is inversely proportional to platelet thickness, $S_s=2/(h \cdot \rho_m)$, bentonite - characterized by its high specific surface area- is used in the following experimental studies to investigate the sediment response to changes in ionic concentration.

Particle migration in an ionic concentration gradient

Diffusiophoresis tests conducted in the petri dish (Figure 1a) show that bentonite particles migrate toward the salt crystal, as indicated by increased opacity near the crystal, while a more translucent annular region develops farther away (Figure 4a). Diffusiophoresis combines two primary mechanisms (Figure 4b). Hydrated Cl^- ions tend to diffuse faster than hydrated Na^+ ions (Lin and Prieve 1983); charge compensation to satisfy local electroneutrality involves both the clay surface charge and its counter ion cloud; then both diffusing ions and suspended clay particles migrate (Morrison 1970, Im and Santamarina 2024). In addition, chemiphoresis arises from the tangential osmotic flow of water parallel to the clay surface dragging particles toward the high salt concentration zone (Lechnick and Shaeiwitz 1984). Digital image correlation between images taken at time = 0 and after 10 minutes shows that the average diffusiophoretic velocity is $\sim 0.6 \mu\text{m/s}$ (see similar reported values in Velegol et al. 2016; PIV image in Figure S2). The final sediment height following crystal dissolution reveals the clay accumulation pattern driven by diffusiophoresis (Figure S3).

In practical settings, diffusiophoresis can drive the migration of fine particles within the pore spaces of soils and rocks when exposed to a concentration gradient. This process may alter permeability and, in some cases, lead to clogging. Relevant scenarios include environmental remediation, saltwater intrusion, low-salinity water flooding, and the long-term performance of clay liners.

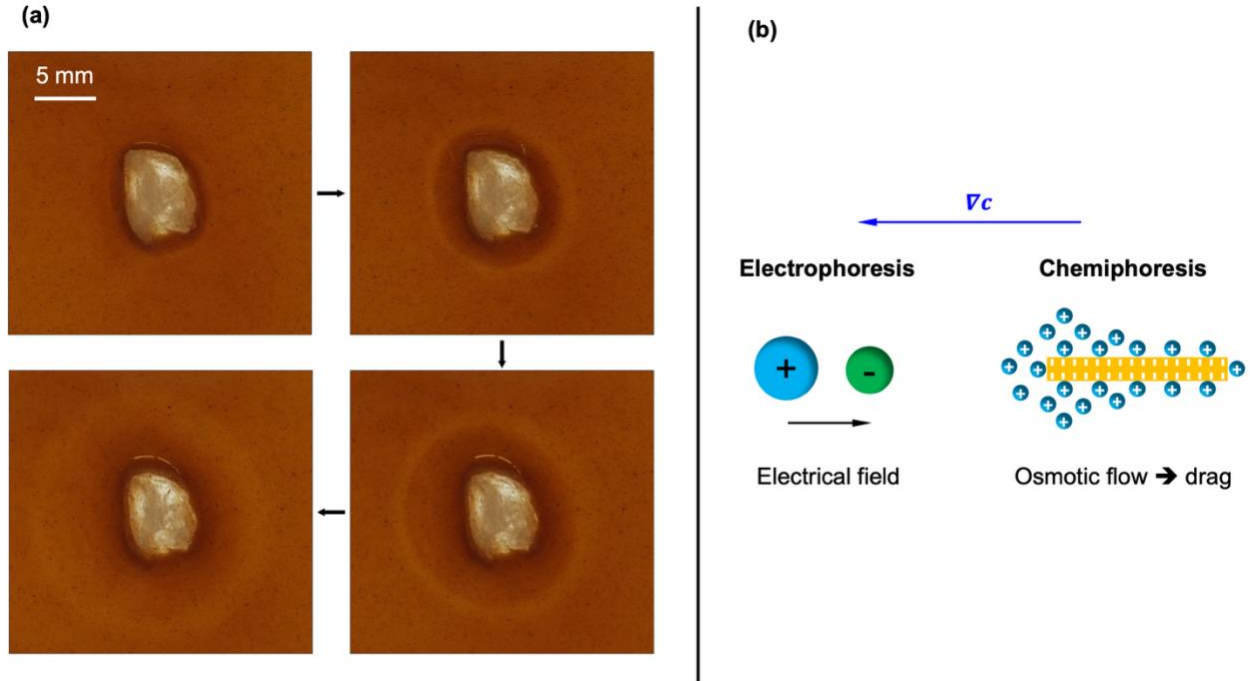


Figure 4. Clay particle migration driven by an ionic concentration gradient - diffusiophoresis. (a) Time-lapse images taken 0, 10, 15, 25 minutes after placing the salt crystal. (b) Diffusiophoresis: negatively charged clay particles migrate towards high ionic concentration zone.

Ionic diffusion through clayey sediments

Once clay particles jam to form a granular skeleton, ion diffusion takes place through the bulk porewater while it interacts with the counter ion cloud around particles. Such intricate processes are particularly relevant to the performance of clay liners (Lake and Rowe 2000, Shackelford and Lee 2003) and in the design of compacted bentonite barriers for nuclear waste storage (Bourg et al. 2006, Miller and Wang 2012, Appelo 2013). Published experimental results on the diffusion of different radionuclides through kaolinite (20 data points) and bentonite sediments (110 data points) were compiled, and the mean interparticle distance \bar{d} [m] was estimated from the reported void ratio e and specific surface area S_s [m^2/g],

$$\bar{d} = \frac{2e}{S_s G_s \rho_w} \quad (5)$$

where the other parameters are the mass density of water $\rho_w = 1000 \text{ kg/m}^3$ the specific gravity of clay minerals $G_s = 2.65$ (Note: the range for crystalline clays 2.45-to-2.85 has second order effect in this

analysis). Figure 5 shows the ratio D_a/D_0 between the apparent diffusion coefficient D_a and the self-diffusion coefficient D_0 plotted against the ratio \bar{d}/d_{ion} between the mean interparticle distance \bar{d} and the ion size d_{ion} . The apparent diffusion coefficient decreases rapidly as the interparticle distance approaches the ion size, $\bar{d}/d_{ion} \rightarrow 1.0$, i.e., ‘pore-throat exclusion’.

In addition to relative pore size \bar{d}/d_{ion} , path tortuosity θ affects diffusion in sediments; combining both effects (Beck and Schultz 1970, Zhao and Burns 2013):

$$D_a = D_0 \cdot \theta \cdot \left[1 - \left(\frac{\bar{d}}{d_{ion}} \right)^{-1} \right]^\alpha \quad (6)$$

Data in Figure 5 plots between the upper bound computed with $\theta = 1$, $\alpha = 4$, and the lower bound computed with $\theta = 0.7$, $\alpha = 20$. The upper bound tracks additional data gathered for porous membranes. Clearly, ion-surface interaction affects ionic diffusion even when the mean pore size is as large as $\bar{d}/d_{ion} > \sim 100$.

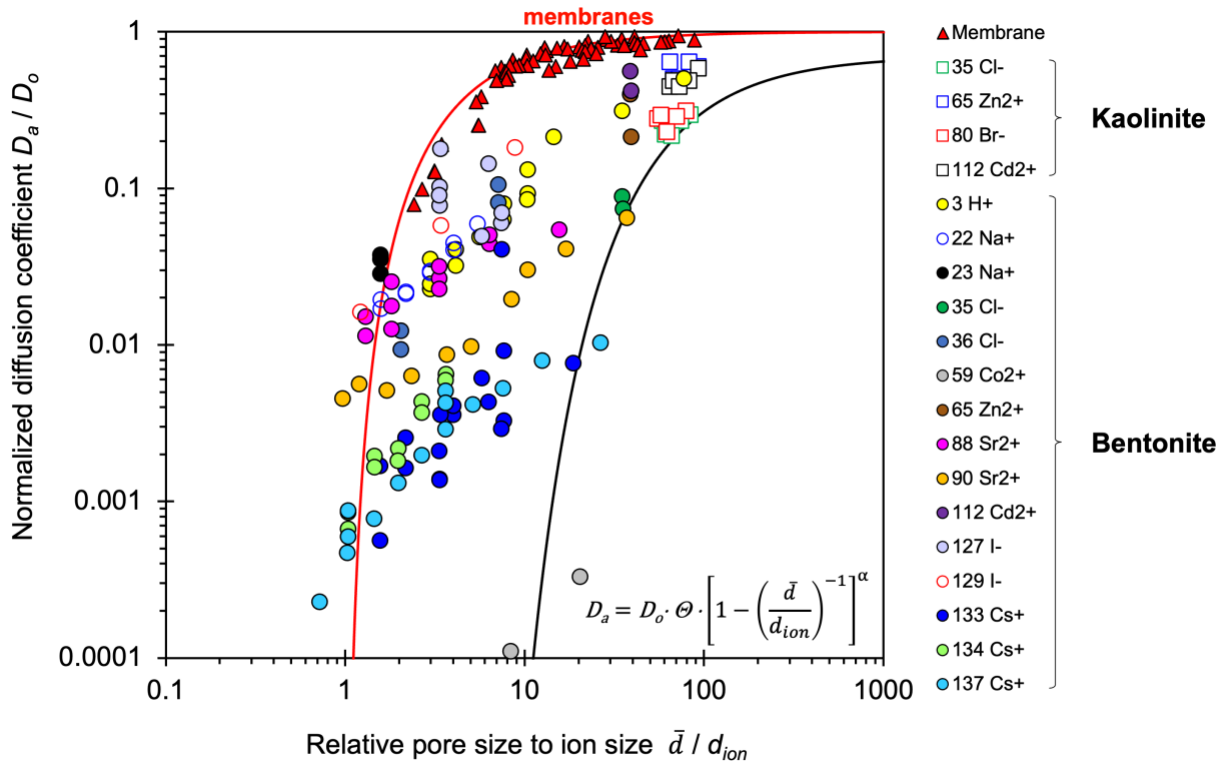


Figure 5. Ionic diffusion through clayey sediments: Pore throat exclusion. Apparent D_a and self diffusion D_0 coefficients. Solid lines: upper and lower bounds computed using the power model (Equation 6). The number preceding each element in the legend denotes its atomic mass number. Data sources: 20 data points

for kaolinite from (Shackelford and Daniel 1991); 110 data points for bentonite from (Shackelford and Daniel 1991, Sato et al. 1992, Kozaki et al. 1996, 1998, 1999, Nakazawa 1999, Molera and Eriksen 2002, Sato 2005); 60 data points for membranes from (Beck and Schultz 1970).

Capillary confinement, osmotic swelling and double layer contraction

Bentonite pastes prepared with deionized water initially swelled upon flooding with salt solutions (Liu et al. 2024). This response may be partly attributed to the suction release when the mixtures are prepared denser than the asymptotic void ratio. Nevertheless, the observation remains puzzling, as it appears to contradict predictions based on DLVO theory, which suggests that increased ionic strength should cause contraction. To investigate the underlying processes, we monitored changes at the sediment-brine interface and internal displacements within the medium.

Grazing incidence X-Ray diffraction GI-XRD tracked the evolution of particles at the interface (Figure 1b). Results show that the interlayer spacing initially *increases* during the first day after flooding with the brine solution, followed by a continuous contraction thereafter for the following 21 days (Figure 6 - The same test sequence was repeated, and identical results were obtained; Figure S4).

Micro-CT imaging (Figure 1c), combined with digital image correlation (particle image velocimetry PIV analysis), provides measurements of internal vertical displacements (Figure 7a). The displacement of each layer reflects the cumulative strain experienced by the sediment beneath it. As shown in Figure 7a, the results reveal a propagating volume expansion front, followed by a phase of contraction.

The particle-scale GI-XRD measurements and the macro-scale CT-based displacement field suggest the following sequence of events (Figure 7b). Before flooding, the air-water interfacial tension at the surface confines the paste so that $e_i < e_0$ (capillary confinement). Flooding cancels this confinement and allows for the initial expansion towards the asymptotic void ratio e_0 , probably fulfilled by the preferential transport of water molecules. Eventually, ion diffusion causes double layer contraction, and settlement takes place. The time needed for ion diffusion is longer than water invasion due to semi-permeable osmotic effects, hence, there is early volume expansion. The time scale of tests conducted in the tomographer correspond to water

transport and ion diffusion into the bentonite pastes (a few days in Figure 7), whereas the longer time scales observed in GI-XRD tests indicate relatively slow interlayer equilibration processes (three weeks in Figure 6).

Concurrent suction release and changes in ionic strength affect a wide range of geotechnical systems, including dams, coastal protection systems, embankments and clay liners. These experimental observations can help guide the design of tests and the interpretation of results in compaction-flooding sequences, particularly when expansive soils are involved.

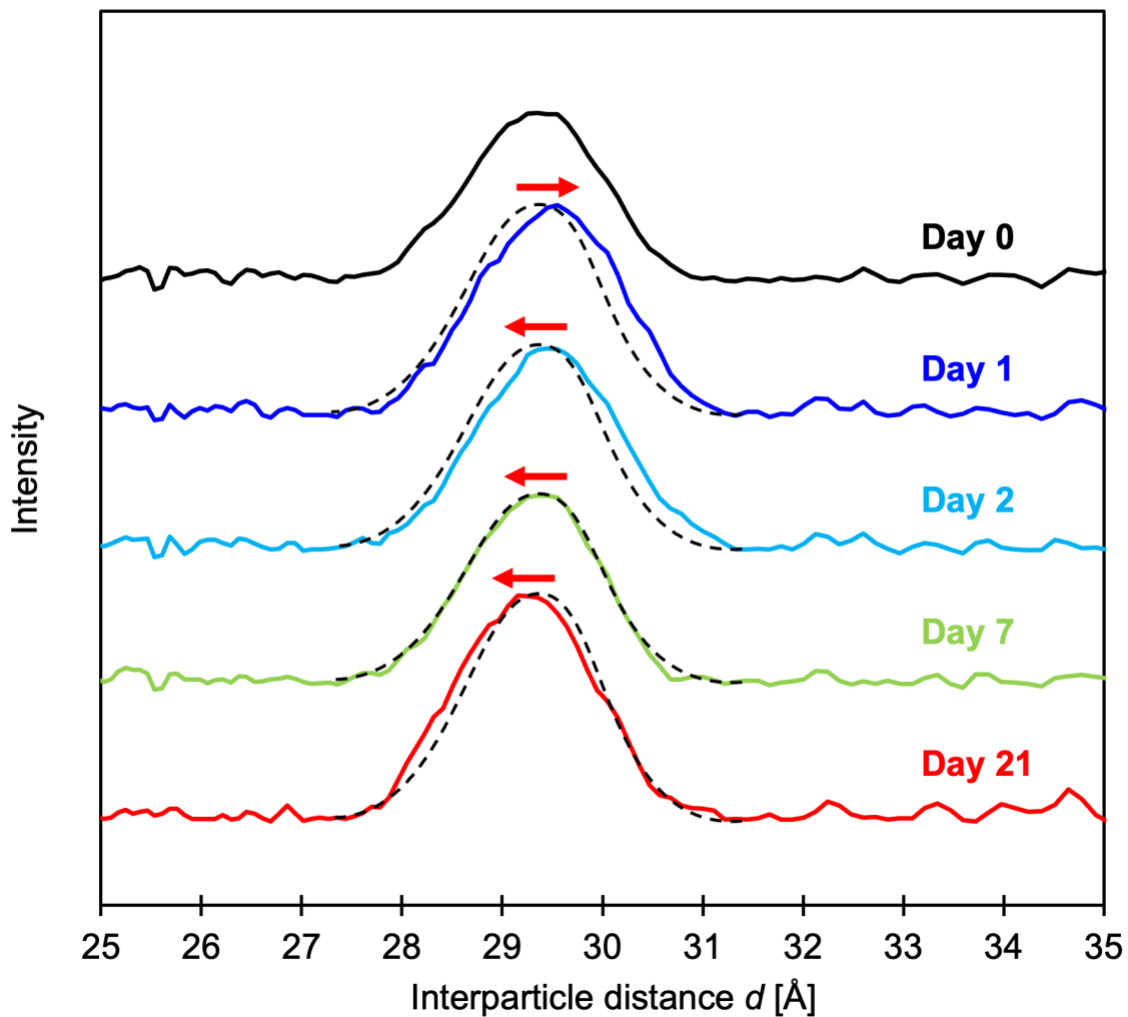


Figure 6. Evolution of interlayer spacing after brine flooding – bentonite particles at the sediment-brine interface (Grazing incidence X-Ray diffraction GI-XRD - Figure 1b). Results show an initial increase in interlayer spacing followed by a continuous contraction thereafter for the following 21 days.

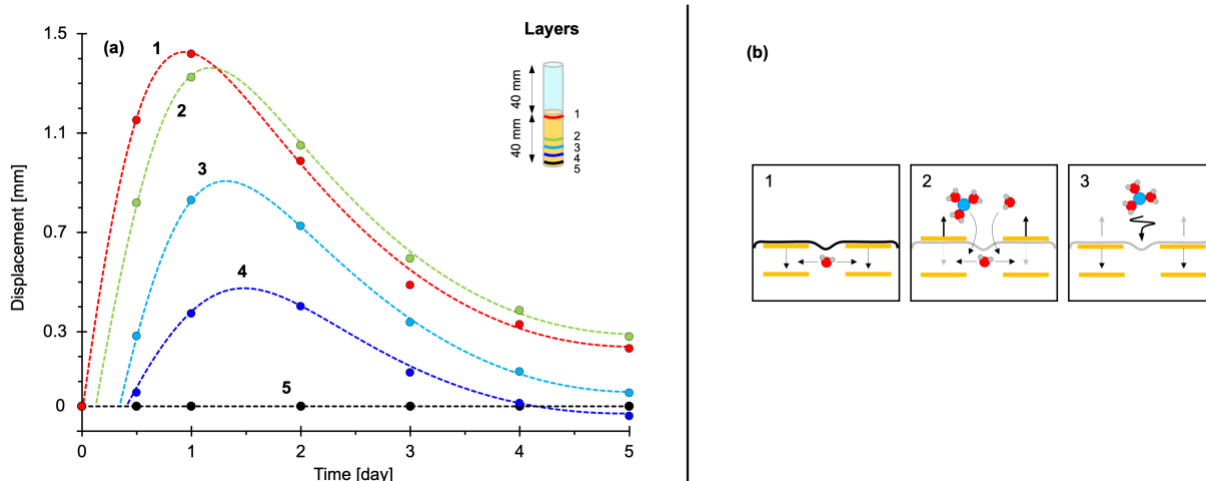


Figure 7. Internal particle displacements in a bentonite sediment following saltwater flooding, based on digital image correlation PIV analysis of sequential high-resolution X-ray tomograms. (a) Particle displacement at different depths show a propagating front with an initial volume expansion phase followed by contraction. (b) Underlying physical phenomena: 1. capillary confinement, 2. preferential water invasion and expansion, and 3. ionic diffusion and contraction.

Changes in pore size distribution

Soft, high surface area clays eventually contract during the diffusion of a high ionic concentration front. What are the internal changes in pore size distribution? Nuclear magnetic resonance NMR spectra provides unprecedented information about pore size distribution and changes associated to the pore fluid chemistry (protocol described above – Figure 1d&e).

Figure 8a compares T_2 relaxation spectra collected before flooding and nine days after flooding with the 0.25 M NaCl solution (Figure 1d). The peak at $T_2 \approx 2$ ms corresponds to adsorbed water, while the peak at $T_2 \approx 10$ –50 ms is associated with the relaxation of bulk water within pores. The persistence of both peaks after diffusion confirms that the pore structure remained largely unchanged, despite the minor contraction driven by ionic diffusion ($\epsilon_{vol} < 1\%$).

On the right hand, Figure 8b presents the T_2 relaxation spectra for two specimens mixed with either deionized DI-water or brine. The sediment mixed with DI-water exhibits similar peaks to those in Figure 8a (Note: the bulk water peak appears at a higher relaxation time in agreement with the larger void ratio,

i.e., greater pore size). In contrast, the sediment mixed with 1 M NaCl solution shows four distinct peaks. The peak at $T_2 \approx 2500$ ms corresponds to supernatant water above the sediment, consistent with the lower asymptotic void ratio e_0 observed when the slurry is prepared with brine (Figure 3). The remaining three peaks suggest a greater diversity of particle associations and more complex pore structures, consistent with the fabric map in Figure 2b.

These experiments demonstrate that changes in ionic concentration during diffusion do not lead to significant clay reassembly, even in very soft sediments subjected to $\sigma' \approx 0$, indicating notable stability of the initial structure formed during self-assembly. However, the introduction of external energy such as mechanical mixing, can overcome the energy barrier required for structural reorganization. Collectively, these findings suggest that soil pore structure retains a "memory" of its chemo-hydro-mechanical history.

In geotechnical practice, these findings suggest that field conditions governed by slow ionic diffusion, such as seawater intrusion or brine migration around cutoff walls, are likely to produce gradual, diffusion-controlled settlements and only minor changes in hydraulic conductivity. In contrast, scenarios involving chemical alteration combined with high specific energy input, such as turbulent slurry pumping or dredged material deposition, can trigger abrupt fabric reorganization and lead to significant volume change or pore pressure generation. These processes underly the formation and characteristic behaviour of sensitive clays.

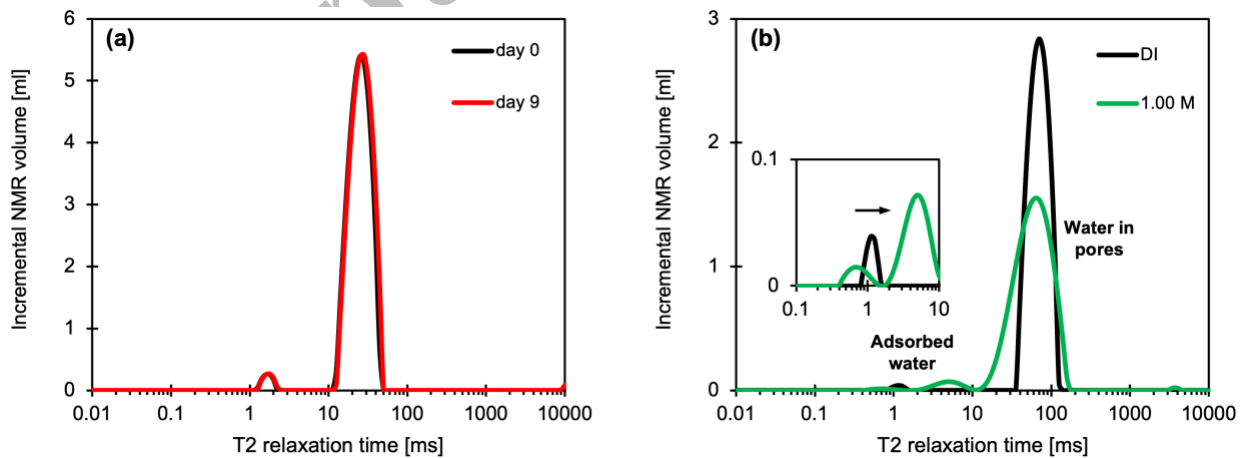


Figure 8. Nuclear magnetic resonance NMR spectra used to assess pore size distribution and changes related to pore fluid chemistry in a bentonite sediment. (a) Quiescent bentonite sediment subjected to salt

diffusion: there are minimal changes in T_2 spectrum. (b) Mixing with DI-water and brine: T_2 spectra exhibit marked differences.

The emergence of subsurface discontinuities

Subsurface discontinuities in sedimentary columns have been observed in both laboratory and field studies (White 1961, Burst 1965, Plummer and Gostin 1981, Pratt 1998, Zhao and Santamarina 2020). However, discontinuities in clay slurries beneath a brine pool remain poorly understood (McMahon et al. 2017). This section explores the underlying mechanisms driving this phenomenon, drawing on experimental evidence from multi-scale and multi-physics tests.

Changes in gas solubility during ionic diffusion → Bubble nucleation and growth. In the field, the pore fluid in saturated sediments contains dissolved gas. The equilibrium gas concentration decreases with increasing salinity, as hydrated ions disrupt the structure of water molecules (Figure 9a). Consequently, a diffusing front of high ionic concentration must cause gas exclusion. Indeed, micro-CT images show bubble nucleation and grain-displacive bubble growth during salt diffusion in a bentonite sediment prepared with deionized, but not deaired water (Figure 9b – Specimen: 50 g/L, initial void ratio $e_a = 53$ – Protocol in Figure 1c). For validation, there is no gas bubble nucleation when slurries are deaired during specimen preparation, prior to brine flooding (tomogram slices in Figure S5).

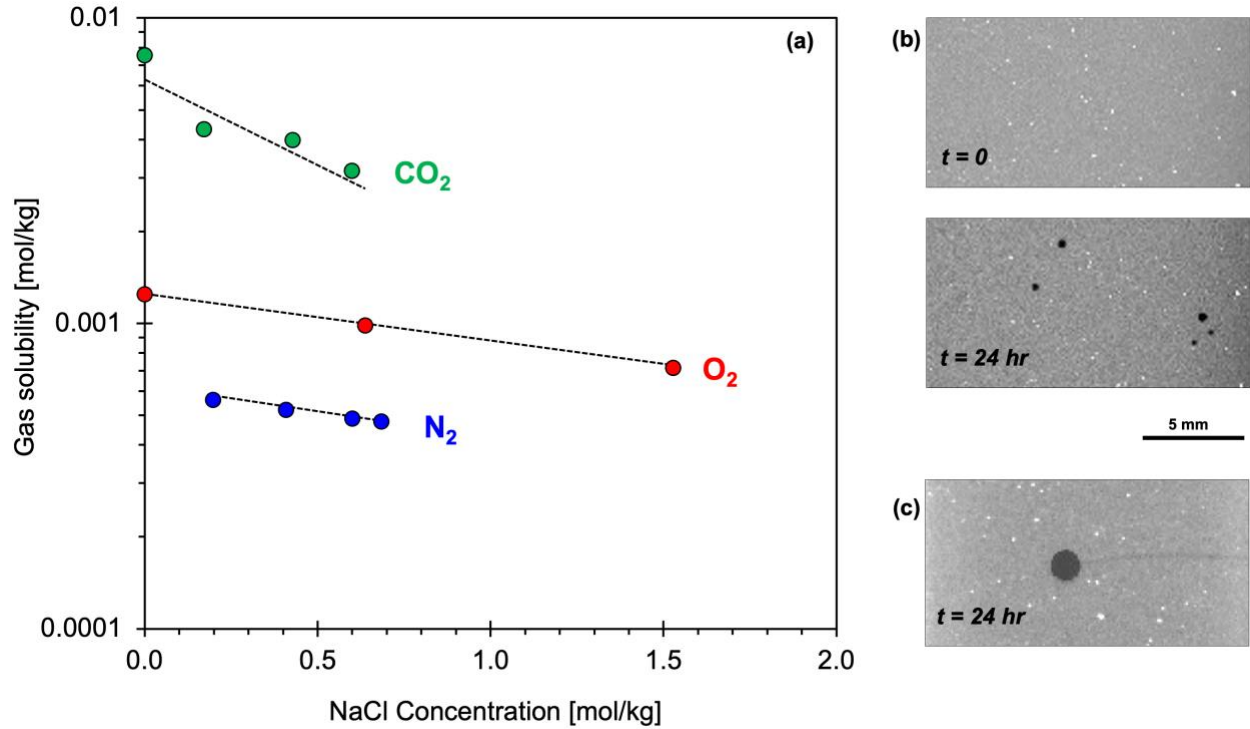


Figure 9. Gas exsolution induced by diffusive ion transport and its consequences. (a) Gas solubility versus NaCl concentration at ambient pressure and temperature (data from (Sun et al. 2001, Al-Anezi et al. 2008, Geng and Duan 2010)). (b) Slices of X-ray tomograms capture the same slice before and after gas bubble nucleation after 24 hours of salt diffusion. (c) This slice shows that grain-displacive gas bubble growth is a nucleation point for a horizontal discontinuity.

Internal horizontal discontinuities. Micro-CT images also reveal that some larger bubbles act as nucleation sites for horizontal discontinuities within the small cylinders (Figure 9c). To investigate discontinuities forming without boundary effects, we conducted tests in the large cylindrical tank (Figure 1f). Since high-resolution X-ray monitoring is not feasible at this scale, we employed acoustic reflection monitoring instead. Figure 10a shows P-wave signatures recorded at the same location over 24 consecutive days:

- The first reflections at $\sim 280 \mu\text{s}$ correspond to the saltwater-sediment interface; while they remain relatively constant, a detailed analysis shows an initial swelling phase followed by contraction.
- Final reflections at $\sim 490 \mu\text{s}$ and $\sim 520 \mu\text{s}$, return from the top and bottom surfaces of the bottom plate.
- The intermediate reflections suggest the emergence and downward migration of horizontal discontinuities within the sediment column (Note: the 3 mm-wavelength P-waves cannot resolve

individual nucleating bubbles).

The phase inversion of P-wave signals reflected from the horizontal discontinuities is consistent with the lower acoustic impedance of water-filled gaps compared to the overlying sediment – See details in the expanded signature recorded after 8.5 days in Figure 10b.

While potentially influenced by boundary effects, horizontal time-lapse photography confirms the formation and gradual downward migration of horizontal discontinuities, as observed through the transparent side wall (Figure 11a). Furthermore, the photographic sequence reveals that the sediment retains a memory of previous discontinuities: expelled water can temporarily reopen previously closed overlying gaps to facilitate drainage before they close again (Figure 11a). This cyclical sequence of formation-closure-reopening-reclosure was observed multiple times, suggesting a hydro-mechanical memory embedded within the sedimentary column.

Finally, it is worth noting that horizontal discontinuities do not form in similar tests conducted with low-plasticity 1:1 kaolinite (Liu et al. 2024).

Vertical discontinuities. Meanwhile, vertically aligned cameras captured the formation and gradual widening of vertical discontinuities on the surface of the bentonite sediment (Figure 11b).

Overall analysis. Vertical discontinuities can be attributed to double-layer contraction and aggregation induced by salt diffusion under zero lateral strain conditions. However, the mechanisms driving the migration of horizontal discontinuities under constant overburden stress remain unclear. A combined analysis of all experimental observations suggests the following potential sequence of events:

1. Salt diffusion initiates gas exsolution, grain-displacive bubble formation and chemo-contraction of the bentonite sediment (Note: 1:1 clays such as kaolinite do not necessarily form a denser fabric under high ionic concentrations)
2. Excess pore pressure builds up as water is released in the low-permeability sediment if the time scale of pressure diffusion approaches that of chemical diffusion (see pressure measurements Santamarina and Fam 1995)

3. Bubble growth and excess pore pressure along the advancing diffusion front interact to generate horizontal discontinuities (Figure 11c)
4. As excess pore pressure dissipates, existing discontinuities close (Figure 11a), while new ones form deeper within the sediment in response to the continuing advance of the ionic front.

The emergence, migration, and residual memory of open-mode discontinuities in high-plasticity clay barriers exposed to brine intrusion can compromise their sealing effectiveness. As a result, chemo-hydro-mechanical coupling must be explicitly considered in the design and performance monitoring of clay-based barriers used in chemically aggressive environments. These include cut-off walls, clay liners in waste containment systems, bentonite cushions in tailings storage facilities, and deep-mixing columns beneath embankments.

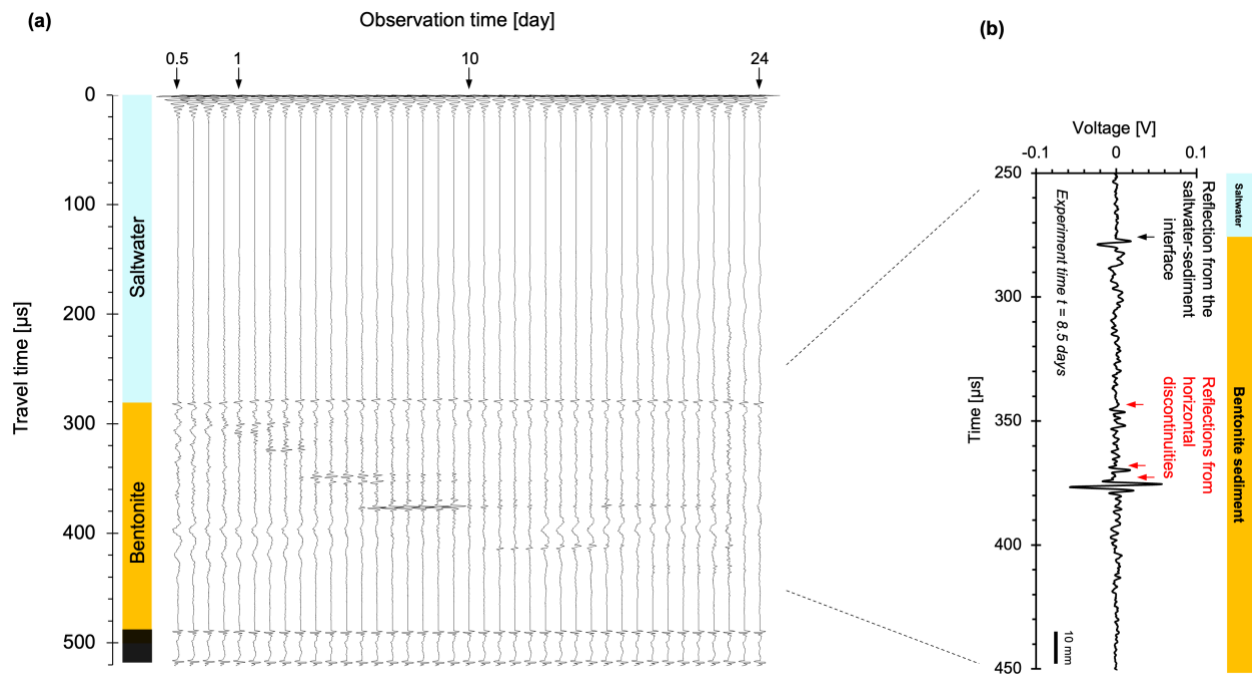


Figure 10. Emergence and downward migration of horizontal discontinuities within the sediment column during ionic diffusion into a stable bentonite sediment (large chamber – Figure 1f). (a) P-wave reflection signatures recorded at the same location over 24 consecutive days: reflections between 300-and-450 μ s show the formation and downward migration of horizontal discontinuities. (b) Phase inversion of P-wave signatures confirms lower impedance in the water-filled discontinuities than in the surrounding sediment (P-wave signature gathered at 8.5 Days).

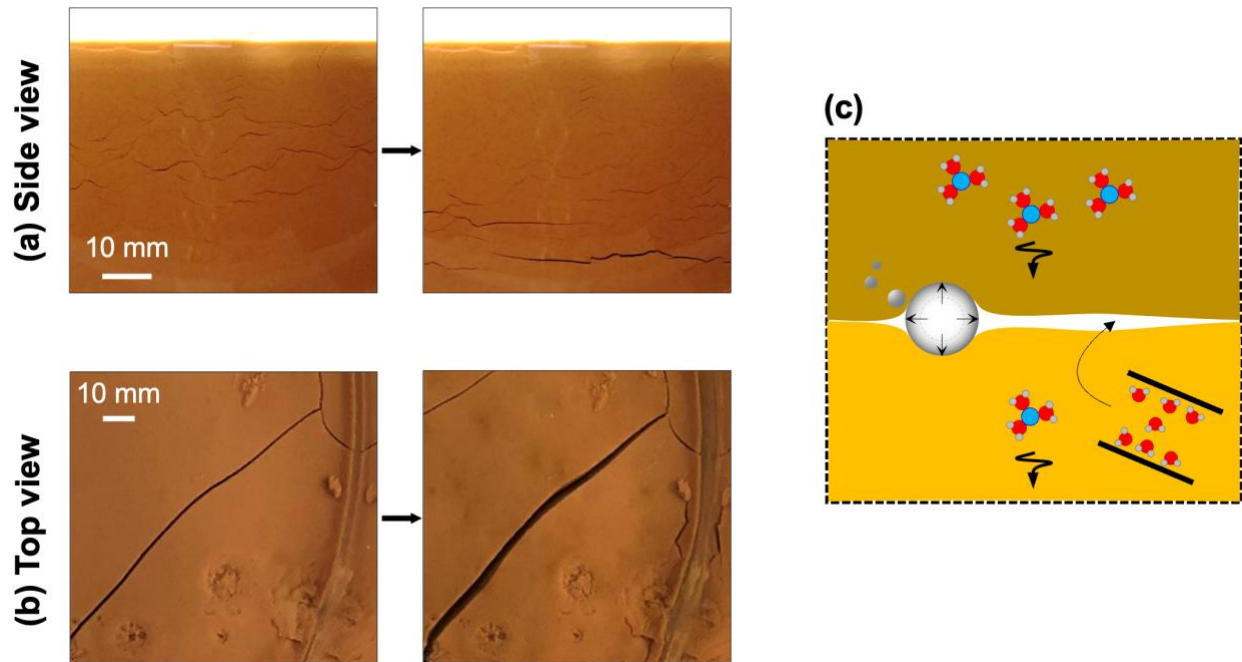


Figure 11. Formation and evolution of internal discontinuities in a bentonite sediment subjected to ionic diffusion – Time-lapse photographs (Test configuration in Figure 1f). (a) Lateral photographs confirm the migration of horizontal discontinuities (as observed through the transparent chamber). (b) Vertical photographs show persistent, contraction-driven vertical discontinuities. (c) Grain-displacive bubble growth as a nucleator for discontinuities (refer to Figure 9c).

Accepted Manuscript

DISCUSSION – OTHER GEOTECHNICAL IMPLICATIONS

Our focus on soft sediments prepared with high specific surface area bentonite reflects the need to induce measurable responses within relatively small laboratory specimens. Chemo-mechanical coupling effects diminish in clays with lower specific surface area and under higher effective stress. However, even minor strains can accumulate over time in large-scale engineering applications, potentially giving rise to phenomena observed in this study, including the formation of discontinuities.

Notably, the invasion of a high ionic strength fluid into soils under zero lateral strain boundary conditions ($\varepsilon_x = \varepsilon_y = 0$) leads to vertical contraction ($\varepsilon_z > 0$), a reduction in lateral effective stress (which can induce shear failure or even vertical open discontinuities as observed here), and a decrease in horizontal permeabilities k_x and k_y yet with an increase in vertical permeability k_z . In contrast, fluid exchange under constant lateral stress, as in standard triaxial testing, produces different chemo-mechanical responses. This underscores the importance of carefully selecting boundary conditions in both laboratory studies and engineering analyses.

Although the experiments presented here focused on clay beds, the underlying particle-scale processes are equally applicable to clay particles residing within the pore spaces of silts, sands, and fractured rocks. For example, low-salinity water flooding can induce dispersion, promote fines migration and lead to clogging, while a low-pH water front tends to promote clay particle aggregation thereby reducing fines migration. These processes are relevant not only to near-surface geotechnical applications but also to deeper energy geotechnology contexts, such as resource recovery and CO₂ geological storage.

CONCLUSIONS

This study investigated the self-assembly of clay particles and the near-surface sediment response to changes in pore fluid salinity. Salient conclusions from this study follow:

- The self-assembly of clay particles is determined by the fluid pH and ionic strength. Previous fabric maps were based on macroscale measurements. The revised fabric maps for 1:1 kaolinite and 2:1 montmorillonite use atomic-scale measurements, numerical simulation results, and DLVO analysis. These maps reveal distinct particle associations in the pH-concentration space with well-defined thresholds.
- For simple reference values, consider: (1) seawater concentration ~ 0.7 mol/L shields surface charges and promotes aggregation of all kinds; (2) the ionic concentration in freshwater is low < 0.01 mol/L (rain, rivers, lakes and most groundwater), and self-assembly windows are defined by pH-dependent surface and edge charges; (3) at low ionic concentration, expect marked transitions in fabric at pH = 5- to-6.5.
- The *ab initio* void ratio at the onset of sediment formation is determined by particle self-assembly and defines the asymptotic void ratio e_0 when the suspension transitions to a sediment as $\sigma' \rightarrow 0$. Pore fluid chemistry, mineralogy, specific surface area (particle thickness), and particle slenderness determine the asymptotic void ratio for fine-grained platy sediments.
- A saturated soil mass surrounded by air experiences capillary confinement when the void ratio is lower than the asymptotic void ratio e_0 , even in high water content pastes. In such cases, soils will swell toward the asymptotic void ratio once capillary forces are released upon flooding. Eventually, the sediment tends to contract if the flooding fluid has high ionic concentration.
- Fine clay particles can migrate against an ionic concentration gradient, driven by the electrical field generated by differences in ion diffusion rates and the drag induced by osmotic pressure.
- While tortuosity reduces the effective ionic diffusion rate, pore size plays a governing role in hindering ionic transport in clays. Pore-throat exclusion becomes increasingly noticeable as the mean pore size

decreases below ~ 100 times the diameter of the diffusing ion.

- Nuclear Magnetic Resonance provides exceptional insight into pore size distribution and its evolution during chemical fronts and mixing. While salt diffusion induces volumetric strain, the pore size distribution remains largely unchanged, hinting at the remarkable stability of self-assembled particle associations. External energy is needed to overcome the energy barrier required for fabric reassembly and changes in pore topology. As a result, the current pore structure of a soil reflects its hydro-chemo-mechanical history.
- Various discontinuities may emerge in soft clay sediments during the diffusion of a high-concentration ionic front. Most surprising are horizontal discontinuities: they nucleate at grain-displacive gas bubbles that form as a result of gas exclusion ahead of the advancing concentration front, and they remain open while water expelled by skeletal contraction drains out.
- Self-assembly, fabric effects, and strains induced by changes in pore fluid chemistry are responsible for a wide range of geotechnical phenomena, including: soil dispersion and internal erosion, quick clay formation, rainfall-induced surface erosion, settlement due to saltwater intrusion in coastal plains, fines migration and clogging, and contraction of clay liners exposed to leachate along with the potential emergence of discontinuities. These chemo-mechanical effects depend on boundary conditions and must be carefully considered in both experimental protocols and engineering design.

ACKNOWLEDGMENTS

Support for this research was provided by the KAUST Endowment at King Abdullah University of Science and Technology, and the GW Clough Endowed Chair at Georgia Tech. The authors thank Youyou Yuan (KAUST Imaging and Characterization Core Lab) for assistance with the GI-XRD experiments.

Accepted manuscript

REFERENCES

- Al-Anezi, K., Somerfield, C., Mee, D., and Hilal, N. 2008. Parameters affecting the solubility of carbon dioxide in seawater at the conditions encountered in MSF desalination plants. *Desalination*, **222**(1–3): 548–571. Elsevier.
- Anderson, J.L. 1989. Colloid transport by interfacial forces. *Annual review of fluid mechanics*, **21**(1): 61–99. Annual Reviews 4139 El Camino Way, PO Box 10139, Palo Alto, CA 94303-0139, USA.
- Appelo, C.A.J. 2013. A review of porosity and diffusion in bentonite. Posiva Oy.
- Bachus, R.C., and Santamarina, J.C. 2014. Geotechnical properties and diagenesis of ponded fly ash. *In Geo-Congress 2014: Geo-characterization and Modeling for Sustainability*. pp. 326–333.
- Barbour, S.L. 1987. Osmotic flow and volume change in clay soils. University of Saskatchewan.
- Bauer, E. 1996. Calibration of a comprehensive hypoplastic model for granular materials. *Soils and foundations*, **36**(1): 13–26. The Japanese Geotechnical Society.
- Beck, R.E., and Schultz, J.S. 1970. Hindered diffusion in microporous membranes with known pore geometry. *Science*, **170**(3964): 1302–1305. American Association for the Advancement of Science.
- Bergström, L. 1997. Hamaker constants of inorganic materials. *Advances in colloid and interface science*, **70**: 125–169. Elsevier.
- Bourg, I.C., Sposito, G., and Bourg, A.C.M. 2006. Tracer diffusion in compacted, water-saturated bentonite. *Clays and Clay Minerals*, **54**(3): 363–374. Cambridge University Press & Assessment.
- Bourg, I.C., Sposito, G., and Bourg, A.C.M. 2007. Modeling the acid–base surface chemistry of montmorillonite. *Journal of Colloid and Interface Science*, **312**(2): 297–310. Elsevier.
- Burst, J.F. 1965. Subaqueously formed shrinkage cracks in clay. *Journal of Sedimentary Research*, **35**(2). Society for Sedimentary Geology.
- Chang, J., Shao, H., Liu, B., Manica, R., Li, Z., Liu, Q., and Xu, Z. 2021. Control of nanostructures through pH-dependent self-assembly of nanoplatelets. *Journal of Colloid and Interface Science*, **582**: 439–445. Elsevier.
- Cho, G.-C., Dodds, J., and Santamarina, J.C. 2006. Particle shape effects on packing density, stiffness, and strength: natural and crushed sands. *Journal of geotechnical and geoenvironmental engineering*, **132**(5): 591–602. American Society of Civil Engineers.
- Chong, S.-H., and Santamarina, J.C. 2016. Soil compressibility models for a wide stress range. *Journal of Geotechnical and Geoenvironmental Engineering*, **142**(6): 06016003. American Society of Civil Engineers.
- Collins, K. t, and McGown, A. 1974. The form and function of microfabric features in a variety of

- natural soils. *Geotechnique*, **24**(2): 223–254. Thomas Telford Ltd.
- Cubrinovski, M., and Ishihara, K. 2002. Maximum and minimum void ratio characteristics of sands. *Soils and foundations*, **42**(6): 65–78. The Japanese Geotechnical Society.
- Ebel, J.P., Anderson, J.L., and Prieve, D.C. 1988. Diffusiophoresis of latex particles in electrolyte gradients. *Langmuir*, **4**(2): 396–406. ACS Publications.
- Elzbiaciak-Wodka, M., Popescu, M.N., Ruiz-Cabello, F., Trefalt, G., Maroni, P., and Borkovec, M. 2014. Measurements of dispersion forces between colloidal latex particles with the atomic force microscope and comparison with Lifshitz theory. *The Journal of chemical physics*, **140**(10). AIP Publishing.
- Farrar, D.M., and Coleman, J.D. 1967. The correlation of surface area with other properties of nineteen British clay soils. *Journal of Soil Science*, **18**(1): 118–124. Wiley Online Library.
- Fuggle, A.R., Roozbahani, M.M., and Frost, J.D. 2014. Size effects on the void ratio of loosely packed binary particle mixtures. *In Geo-Congress 2014: Geo-Characterization and Modeling for Sustainability*. pp. 129–138.
- Geng, M., and Duan, Z. 2010. Prediction of oxygen solubility in pure water and brines up to high temperatures and pressures. *Geochimica et Cosmochimica Acta*, **74**(19): 5631–5640. Elsevier.
- Goodall, T.M., North, C.P., and Glennie, K.W. 2000. Surface and subsurface sedimentary structures produced by salt crusts. *Sedimentology*, **47**(1): 99–118. Wiley Online Library.
- Gupta, V., Hampton, M.A., Stokes, J.R., Nguyen, A. V, and Miller, J.D. 2011. Particle interactions in kaolinite suspensions and corresponding aggregate structures. *Journal of Colloid and Interface Science*, **359**(1): 95–103. Elsevier.
- Gupta, V., and Miller, J.D. 2010. Surface force measurements at the basal planes of ordered kaolinite particles. *Journal of Colloid and Interface Science*, **344**(2): 362–371. Elsevier.
- Hansen, B. 1969. A mathematical model for creep phenomena in clay. *Advances in consolidation theories for clays*,: 12–18. Univ. of Waterloo, Faculty of Engineering Waterloo, ON, Canada.
- Hong, Z.-S., Yin, J., and Cui, Y.-J. 2010. Compression behaviour of reconstituted soils at high initial water contents. *Géotechnique*, **60**(9): 691–700. Thomas Telford Ltd.
- Im, J., and Santamarina, J.C. 2024. Understanding the limits of binary diffusion for enhanced clay barrier design. *PNAS nexus*, **3**(9): pga366. Oxford University Press US.
- Imai, G. 1981. Experimental studies on sedimentation mechanism and sediment formation of clay materials. *Soils and foundations*, **21**(1): 7–20. The Japanese Geotechnical Society.
- Israelachvili, J.N. 1978. Measurement of forces between surfaces immersed in electrolyte solutions. *Faraday Discussions of the Chemical Society*, **65**: 20–24. Royal Society of Chemistry.
- Israelachvili, J.N. 2011. *Intermolecular and surface forces*. Academic press.
- Kar, G., Chander, S., and Mika, T.S. 1973. The potential energy of interaction between dissimilar electrical double layers. *Journal of colloid and interface science*, **44**(2): 347–355. Elsevier.
- Klein, K., and Santamarina, J.C. 2005. *Soft sediments: Wave-based characterization*. International

- journal of geomechanics, **5**(2): 147–157. American Society of Civil Engineers.
- Kozaki, T., Fujishima, A., Sato, S., and Ohashi, H. 1998. Self-diffusion of sodium ions in compacted sodium montmorillonite. *Nuclear Technology*, **121**(1): 63–69. Taylor & Francis.
- Kozaki, T., Sato, H., Fujishima, A., Sato, S., and Ohashi, H. 1996. Activation energy for diffusion of cesium in compacted sodium montmorillonite. *Journal of Nuclear Science and Technology*, **33**(6): 522–524. Taylor & Francis.
- Kozaki, T., Sato, Y., Nakajima, M., Kato, H., Sato, S., and Ohashi, H. 1999. Effect of particle size on the diffusion behavior of some radionuclides in compacted bentonite. *Journal of Nuclear Materials*, **270**(1–2): 265–272. Elsevier.
- Lake, C.B., and Rowe, R.K. 2000. Diffusion of sodium and chloride through geosynthetic clay liners. *Geotextiles and Geomembranes*, **18**(2–4): 103–131. Elsevier.
- Lechnick, W.J., and Shaeiwitz, J.A. 1984. Measurement of diffusiophoresis in liquids. *Journal of colloid and interface science*, **102**(1): 71–87. Elsevier.
- Lee, J.-S., and Santamarina, J.C. 2005. P-wave reflection imaging. *Geotechnical testing journal*, **28**(2): 197–206. ASTM International.
- Lin, M.M.-J., and Prieve, D.C. 1983. Electromigration of latex induced by a salt gradient. *Journal of colloid and interface science*, **95**(2): 327–339. Elsevier.
- Liu, J., Miller, J.D., Yin, X., Gupta, V., and Wang, X. 2014. Influence of ionic strength on the surface charge and interaction of layered silicate particles. *Journal of colloid and interface science*, **432**: 270–277. Elsevier.
- Liu, M., Park, J., and Santamarina, J.C. 2024. Stratified water columns: homogenization and interface evolution. *Scientific Reports*, **14**(1): 11453. Nature Publishing Group UK London.
- Lyu, C., Park, J., and Carlos Santamarina, J. 2021. Depth-dependent seabed properties: Geoacoustic assessment. *Journal of Geotechnical and Geoenvironmental Engineering*, **147**(1): 04020151. American Society of Civil Engineers.
- Di Maio, C. 1996. Exposure of bentonite to salt solution: osmotic and mechanical effects. *Géotechnique*, **46**(4): 695–707. Thomas Telford Ltd.
- Masliyah, J.H., and Bhattacharjee, S. 2006. *Electrokinetic and colloid transport phenomena*. John Wiley & Sons.
- McMahon, S., van Smeerdijk Hood, A., and McIlroy, D. 2017. The origin and occurrence of subaqueous sedimentary cracks.
- Mesri, G., and Olson, R.E. 1971. Consolidation characteristics of montmorillonite. *Geotechnique*, **21**(4): 341–352. Thomas Telford Ltd.
- Miller, A.W., and Wang, Y. 2012. Radionuclide interaction with clays in dilute and heavily compacted systems: a critical review. *Environmental science & technology*, **46**(4): 1981–1994. ACS Publications.
- Mitchell, J.K., and Soga, K. 2005. *Fundamentals of soil behavior*. John Wiley & Sons New York.

- Mohammed, I., Al Shehri, D., Mahmoud, M., Kamal, M.S., and Alade, O.S. 2021. A surface charge approach to investigating the influence of oil contacting clay minerals on wettability alteration. *ACS omega*, **6**(19): 12841–12852. ACS Publications.
- Molera, M., and Eriksen, T. 2002. Diffusion of $^{22}\text{Na}^+$, $^{85}\text{Sr}^{2+}$, $^{134}\text{Cs}^+$ and $^{57}\text{Co}^{2+}$ in bentonite clay compacted to different densities: experiments and modeling. *Radiochimica Acta*, **90**(9–11): 753–760. De Gruyter Oldenbourg.
- Morrison, F.A. 1970. Electrophoresis of a particle of arbitrary shape. *Journal of Colloid and Interface Science*, **34**(2): 210–214. Elsevier.
- Musso, G., Scelsi, G., and Della Vecchia, G. 2022. Chemo-mechanical behaviour of non-expansive clays accounting for salinity effects. *Géotechnique*, **74**(7): 632–646. Emerald Publishing Limited.
- Nakazawa, T. 1999. Activation energies of diffusion of tritium and electrical conduction in water-saturated compacted sodium montmorillonite. *Proc. Radioactive Waste Management and Environmental Remediation, 1999*,. ASME.
- O'Brien, N.R. 1971. Fabric of kaolinite and illite floccules. *Clays and Clay Minerals*, **19**(6): 353–359. Cambridge University Press & Assessment.
- van Olphen, H. 1964. An introduction to clay colloid chemistry. *Soil Science*, **97**(4): 290. LWW.
- Palomino, A.M., and Santamarina, J.C. 2005. Fabric map for kaolinite: Effects of pH and ionic concentration on behavior. *Clays and Clay minerals*, **53**(3): 211–223. Cambridge University Press & Assessment.
- Plummer, P.S., and Gostin, V.A. 1981. Shrinkage cracks; desiccation or syneresis? *Journal of Sedimentary Research*, **51**(4): 1147–1156. SEPM Society for Sedimentary Geology.
- Pratt, B.R. 1998. Molar-tooth structure in Proterozoic carbonate rocks: origin from synsedimentary earthquakes, and implications for the nature and evolution of basins and marine sediment. *Geological Society of America Bulletin*, **110**(8): 1028–1045. Geological Society of America.
- Prieve, D.C., Anderson, J.L., Ebel, J.P., and Lowell, M.E. 1984. Motion of a particle generated by chemical gradients. Part 2. Electrolytes. *Journal of Fluid Mechanics*, **148**: 247–269. Cambridge University Press.
- Rand, B., and Melton, I.E. 1977. Particle interactions in aqueous kaolinite suspensions: I. Effect of pH and electrolyte upon the mode of particle interaction in homoionic sodium kaolinite suspensions. *Journal of Colloid and Interface Science*, **60**(2): 308–320. Elsevier.
- Randolph, M., and Gourvenec, S. 2017. *Offshore geotechnical engineering*. CRC press.
- Riboulot, V., Ker, S., Sultan, N., Thomas, Y., Marsset, B., Scalabrin, C., Ruffine, L., Boulart, C., and Ion, G. 2018. Freshwater lake to salt-water sea causing widespread hydrate dissociation in the Black Sea. *Nature communications*, **9**(1): 117. Nature Publishing Group UK London.
- Richardson, M.D., and Briggs, K.B. 1993. On the use of acoustic impedance values to determine sediment properties. *In Proc. IOA Vol. pp.* 19–93.

- Roberts, D.A., Johnston, E.L., and Knott, N.A. 2010. Impacts of desalination plant discharges on the marine environment: A critical review of published studies. *Water research*, **44**(18): 5117–5128. Elsevier.
- Rosenqvist, I.T. 1953. Considerations on the sensitivity of Norwegian quick-clays. *Geotechnique*, **3**(5): 195–200. Thomas Telford Ltd.
- Russell, E.R., and Mickle, J.L. 1970. Liquid limit values by soil moisture tension. *Journal of the Soil Mechanics and Foundations Division*, **96**(3): 967–989. American Society of Civil Engineers.
- Salva, R.M., Park, J., Terzariol, M., Jiang, J., and Santamarina, J.C. 2023. Shallow seafloor sediments: Density and shear wave velocity. *Journal of Geotechnical and Geoenvironmental Engineering*, **149**(5): 04023022. American Society of Civil Engineers.
- Santamarina, J.C., and Fam, M. 1995. Changes in dielectric permittivity and shear wave velocity during concentration diffusion. *Canadian Geotechnical Journal*, **32**(4): 647–659. NRC Research Press Ottawa, Canada.
- Santamarina, J.C., Klein, A., and Fam, M.A. 2001. Soils and waves: Particulate materials behavior, characterization and process monitoring. *Journal of Soils and Sediments*, **1**(2): 130. Springer Nature BV.
- Santamarina, J.C., Klein, K.A., Palomino, A., and Guimaraes, M.S. 2002. Micro-scale aspects of chemical-mechanical coupling: Interparticle forces and fabric. *In* Chemo-mechanical coupling in clays: from nano-scale to engineering applications. Routledge. pp. 47–58.
- Sato, H. 2005. Effects of the orientation of smectite particles and ionic strength on diffusion and activation enthalpies of I⁻ and Cs⁺ ions in compacted smectite. *Applied Clay Science*, **29**(3–4): 267–281. Elsevier.
- Sato, H., Ashida, T., Kohara, Y., Yui, M., and Sasaki, N. 1992. Effect of dry density on diffusion of some radionuclides in compacted sodium bentonite. *Journal of Nuclear Science and Technology*, **29**(9): 873–882. Taylor & Francis.
- Schroeder, A., Wiesner, M.G., and Liu, Z. 2015. Fluxes of clay minerals in the South China Sea. *Earth and Planetary Science Letters*, **430**: 30–42. Elsevier.
- Shackelford, C.D., and Daniel, D.E. 1991. Diffusion in saturated soil. II: Results for compacted clay. *Journal of Geotechnical Engineering*, **117**(3): 485–506. American Society of Civil Engineers.
- Shackelford, C.D., and Lee, J.-M. 2003. The destructive role of diffusion on clay membrane behavior. *Clays and Clay Minerals*, **51**(2): 186–196. Cambridge University Press & Assessment.
- Sridharan, A., and Prakash, K. 2001. Settling behaviour and clay mineralogy. *Soils and Foundations*, **41**(2): 105–109. Elsevier.
- Studds, P.G., Stewart, D.I., and Cousens, T.W. 1998. The effects of salt solutions on the properties

- of bentonite-sand mixtures. *Clay Minerals*, **33**(4): 651–660. Cambridge University Press.
- Sun, R., Hu, W., and Duan, Z. 2001. Prediction of nitrogen solubility in pure water and aqueous NaCl solutions up to high temperature, pressure, and ionic strength. *Journal of solution chemistry*, **30**: 561–573. Springer.
- Valmacco, V., Elzbieciak-Wodka, M., Herman, D., Trefalt, G., Maroni, P., and Borkovec, M. 2016. Forces between silica particles in the presence of multivalent cations. *Journal of colloid and interface science*, **472**: 108–115. Elsevier.
- Velegol, D., Garg, A., Guha, R., Kar, A., and Kumar, M. 2016. Origins of concentration gradients for diffusiophoresis. *Soft matter*, **12**(21): 4686–4703. Royal Society of Chemistry.
- Weber, C., and Kaufhold, S. 2021. Hamaker functions for kaolinite and montmorillonite. *Colloid and Interface Science Communications*, **43**: 100442. Elsevier.
- White, W.A. 1961. Colloid phenomena in sedimentation of argillaceous rocks. *Journal of Sedimentary Research*, **31**(4): 560–570. SEPM Society for Sedimentary Geology.
- Xu, G.-Z., Gao, Y.-F., Hong, Z.-S., and Ding, J.-W. 2012. Sedimentation behavior of four dredged slurries in China. *Marine Georesources & Geotechnology*, **30**(2): 143–156. Taylor & Francis.
- Ying, Z., Cui, Y.-J., Duc, M., Benahmed, N., Bessaies-Bey, H., and Chen, B. 2021. Salinity effect on the liquid limit of soils. *Acta Geotechnica*, **16**(4): 1101–1111. Springer.
- Youd, T.L. 1973. Factors controlling maximum and minimum densities of sands. *In Evaluation of relative density and its role in geotechnical projects involving cohesionless soils*. ASTM International.
- Zhao, B., and Santamarina, J.C. 2020. Desiccation crack formation beneath the surface. *Géotechnique*, **70**(2): 181–186. Thomas Telford Ltd.
- Zhao, Q., and Burns, S.E. 2013. Modeling sorption and diffusion of organic sorbate in hexadecyltrimethylammonium-modified clay nanopores—a molecular dynamics simulation study. *Environmental Science & Technology*, **47**(6): 2769–2776. ACS Publications.